Oxygen isotope exchange kinetics between CAI melt and carbon monoxide gas: Implication for CAI formation in the earliest Solar System

Daiki Yamamoto[1], Noriyuki Kawasaki[2], Shogo Tachibana[3,4], Michiru Kamibayashi[3], and Hisayoshi Yurimoto[2]

[1]Department of Earth and Planetary Science, Tokyo Institute of Technology, Ookayama, Tokyo 152-8550, Japan

[2]Department of Natural History Sciences, Hokkaido University, Sapporo, Hokkaido 060-0810, Japan

[3]Department of Earth and Planetary Science, The University of Tokyo, Hongo, Tokyo 113-0033, Japan

[4]Institute of Space and Astronautical Science, Japan Aerospace Exploration Agency, Sagamihara, Kanagawa 252-5210, Japan

Corresponding address: dyamamoto@eps.sci.titech.ac.jp

ABSTRACT

Coarse-grained igneous calcium-aluminum-rich inclusions (CAIs) are suggested to have experienced gas-melt isotope exchange of oxygen during the melting events of their precursors. Therefore, their oxygen isotope variation would preserve information about the high-temperature processes in the earliest Solar System. We experimentally determined oxygen isotope exchange kinetics between CAI analog melt and carbon monoxide (CO) gas at 1420°C and 1460°C under CO gas partial pressures of 0.1, 0.5, and 1 Pa to understand the role of CO gas on the oxygen isotope exchange. We observed oxygen isotope zoning profiles inside the reacted samples that formed through the oxygen isotope exchange reaction at the melt surface and oxygen diffusion in the melt. The zoning profiles were fitted using a three-dimensional spherical diffusion model with time-dependent surface concentration. The oxygen isotope exchange efficiency for colliding CO molecules is estimated to be ~3.3×10^{-4}, which is much smaller than that for H_2O (0.28). The oxygen diffusion coefficient obtained in this study is similar to that obtained in the oxygen isotope exchange experiments between the CAI melt and H_2O, suggesting that the diffusion species in the melt is O^{2-}, despite the surrounding atmospheres.

A comparison of the isotope exchange reaction kinetics between (1) CAI melt and CO gas, (2) CAI melt and H_2O gas, and (3) CO and H_2O gases shows that the reaction rate decreases in the order of (3), (2), and (1). The rapid isotope exchange of the reaction (1) indicates that the oxygen isotopic compositions of H_2O and CO should have been equilibrated during the melting and crystallization processes of igneous CAIs. Both H_2O and CO change the oxygen isotope compositions of molten CAI in the same direction, although reaction (2) controls the isotope exchange timescale between the CAI melt and surrounding gas. Our dataset demonstrates that type B CAIs having melilite with homogeneous oxygen isotope composition should have been heated for 2–3 days at P_{H2} > 100 Pa above the melilite liquidus (~1400°C) in the solar protoplanetary disk.

1. INTRODUCTION

Coarse-grained igneous calcium-aluminum-rich inclusions (CAIs), such as type B CAIs, have an igneous texture that is indicative of the partial melting of their precursor materials condensed from the hot solar composition gas in the earliest Solar System (e.g., Grossman, 1972; Amelin et al., 2002; MacPherson, 2014; Connelly et al., 2012; Kawasaki et al., 2020, 2021). Type B CAIs are mainly composed of spinel, melilite, fassaite, and anorthite (MacPherson, 2014 and references therein). Laboratory experimental simulations using type B CAI analogs have revealed that the precursors of type B CAIs would have been heated at temperatures slightly above the melilite liquidus (~1400°C) and then cooled at rates of ~50–0.1 K h^{-1}, resulting in the crystallization of melilite, followed by fassaite and anorthite (MacPherson et al., 1984; Stolper and Paque, 1986; Mendybaev et al., 2006; Kamibayashi et al., 2021; Yamamoto et al., 2021).

The oxygen isotope compositions of igneous CAIs exhibit mass-independent isotopic distribution among their constituent minerals (e.g., Clayton et al., 1977; Yurimoto et al., 2008 and references therein), and such a disequilibrium distribution of oxygen isotope compositions in CAIs would be caused by oxygen isotope mixing among isotopically distinct reservoirs present in the early Solar System (Yurimoto and Kuramoto, 2004; Lyons and Young, 2005). One of the plausible mechanisms for the mineral-dependent oxygen isotope distribution within CAIs is the gas-melt isotope exchange reaction during reheating processes (Clayton, 1993; Yurimoto et al., 1998; Ito et al., 2004; Aléon et al., 2007; Yoshitake et al., 2005; Aléon, 2016; Kawasaki et al., 2015, 2018; Suzumura et al., 2021). The isotopically distinct oxygen isotope reservoirs in the early Solar System (i.e., oxygen isotope exchange partners for CAI melt) are predicted to be ^{16}O-rich CO and ^{16}O-poor H_2O gas as products of CO self-shielding in the protosolar molecular cloud and/or the protosolar disk (Yurimoto and Kuramoto, 2004; Lyons and Young, 2005).

We have experimentally determined the oxygen isotope exchange kinetics between CAI melt and H_2O gas and constrained the heating timescale and lower limit of

79 water vapor pressure for the partial melting experienced by typical type B CAIs
80 (Yamamoto et al., 2021). However, the gas-phase oxygen isotope exchange reaction
81 between CO and H_2O is a very rapid process during the reheating events of igneous CAIs
82 (Alexander, 2004; Lyons et al., 2009) and CO would be present with its abundance almost
83 equal to that of H_2O based on the Solar System abundance of elements (Wood and
84 Hashimoto, 1993; Lodders, 2021). In this context, CO might accelerate the oxygen
85 isotope exchange rate with the CAI melt, and the required heating timescale and
86 surrounding pressure during partial melting of igneous CAIs would be more strictly
87 constrained by the isotope exchange kinetics between the CAI melt and CO. In this study,
88 we performed oxygen isotope exchange experiments between a CAI analog melt and
89 disk-like low-pressure CO gas to determine the isotope exchange kinetics.
90
91 **2. EXPERIMENTS**
92 **2.1 Oxygen isotope exchange experiments between CAI melt and CO gas**
93 The starting material of CAI analog glass, synthesized by heating at 1440°C
94 for ~5–6 h followed by quenching in air, was the same as used for oxygen isotope
95 exchange experiments between CAI melt and H_2O gas by Yamamoto et al. (2021)
96 (hereinafter referred to as CAIB). Its bulk chemical composition was close to that of
97 average type B CAI (Wark, 1979) and the CAI analog glass was used for the
98 crystallization experiments by Stolper (1982) and Stolper and Paque (1986). The glass
99 has a homogeneous elemental composition and contains small spinel crystals (<~10 μm
100 in diameter) that are a stable phase at 1440°C (Stolper, 1982).
101 A spot-focus infrared gold image vacuum furnace equipped with a gas flow
102 system for CO gas was used for the experiments conducted at 1420°C and 1460°C under
103 low pressures of CO gas (P_{CO}) of 0.1, 0.5, and 1 Pa for 52 min–22 h. The furnace consists
104 of a silica glass tube (inner diameter of 2.6 cm, outer diameter of 3.0 cm, and length of
105 14.3 cm), gold-coated ellipsoidal double mirrors with two halogen lamps, a Pirani/cold-
106 cathode vacuum gauge (Pfeiffer PKR360), a quadrupole mass spectrometer (QMS;
107 HORIBASTEC QL-SG01-065-1A), and a pumping system (a turbo-molecular pump and

a scroll pump; HiCube 80 Eco, Pfeiffer Vacuum) (Yamamoto et al., 2021). The furnace was the same as that used in our previous study (Fig. 1 in Yamamoto et al., 2021), but the gas flow system was changed for CO. For the oxygen isotope exchange experiments with CO, we prepared a gas cylinder-containing ^{18}O-enriched CO gas (~98% ^{18}O) synthesized by Taiyo Nippon Sanso Corp. as the source of CO gas. The gas composition of the cylinder was ~97.2% CO, ~2.2% H_2, ~0.6% N_2, and ~22 ppm CO_2 in volume. The gas flow rate was controlled by a mass flow controller (Kofloc 3600).

A CAIB glass spherule (~2.5–2.7 mm in diameter) on a platinum wire loop was suspended in a cylindrical shaped-iridium cell (6 mm inner diameter, 7 mm outer diameter, and 10 mm length) (Yamamoto et al., 2021). CO gas reached the sample through two holes with diameter of 1 mm on both sides and from the top of the cell. The sample cell was located above the tip of a type R (Pt–Pt13Rh) thermocouple that controlled the temperature of the sample. The sample temperature was corrected within ± 5-°C at each P_{CO} against the liquidus temperature of melilite for the melt with CAIB composition (1380°C; Yamamoto et al., 2021)

After the entire system including the CO gas flow line was evacuated down to (3–5) × 10^{-5} Pa of the total pressure by the pumping system, the CAIB sample was preheated for 0.5–1 h at 600°C and 1000°C, both of which were below the solidus temperature of the CAIB (~1100°C; Stolper and Paque, 1986), respectively, to evacuate the residual gas inside the furnace. The sample was then heated from 1000°C to an experimental temperature of 1420°C or 1460°C (i.e., above the liquidus of melilite) in 4 min. The gas supply line was filled with ~1.2 × 10^5 Pa of CO gas from the gas cylinder during the temperature increase from 1000°C to the maximum temperatures to keep the pressure in the line higher than the surrounding atmosphere (~10^5 Pa). CO gas was introduced into the furnace as soon as the sample temperature reached the experimental temperature. The CO gas pressure (P_{CO}) inside the furnace was adjusted by the balance between a flow rate controlled by the mass flow controller and an evacuation rate controlled by the butterfly valve. The flow rates of CO gas was set at 0.4, 1.4, and 2.8

136 cm^3 min^{-1} for the experiments at P_{CO} = 0.1, 0.5, and 1 Pa, respectively. The fluctuation in
137 the P_{CO} during the experiments was less than 10%. After heating at the maximum
138 temperature for−52 min–22 h, the sample was rapidly cooled down below the CAIB
139 solidus in 1 min by turning off the halogen lamps and the supply of CO gas was stopped.
140 The experimental conditions and results are summarized in Tables 1 and 2.
141 In order to investigate the change in the oxygen isotope composition of the
142 gas during the experiments, the gas species inside the furnace were monitored without
143 the CAI melt analog using the QMS. The maximum working total pressure of the QMS
144 is 0.9 Pa, therefore, gas monitoring was conducted at a P_{CO} of 0.1 and 0.5 Pa.
145
146 **2.2 Sample analysis**
147 The analytical procedure used for the samples is similar to that described in
148 Yamamoto et al. (2021). The run products and the starting material mounted into epoxy
149 resin were polished with a diamond polishing disk with a roughness of 53 μm until the
150 exposed area reached its maximum extent, which was visually evaluated. The center of
151 the cross-section was defined as the center of the sample. The cross section was then
152 carefully polished using diamond pastes down to 1 μm. Observations and phase
153 identification in the cross-section of the samples were conducted using a field emission
154 scanning electron microscope (FE-SEM) (JEOL JSM-7000F at the University of Tokyo
155 and Hokkaido University and Hitachi-SU6600 at the Institute of Space and Astronautical
156 Science, Japan Aerospace Exploration Agency). The chemical compositions of the glass
157 in the run products and the starting material in the polished section were measured using
158 an electron probe micro analyzer (EPMA) (JEOL JXA-8900L) with a wavelength-
159 dispersive X-ray spectrometer (WDS) at the University of Tokyo. Synthetic periclase
160 (MgO), corundum (Al_2O_3), wollastonite ($CaSiO_3$), and ilmenite ($FeTiO_3$) were used as
161 standards for quantitative EPMA analysis. Because the glass was chemically
162 homogeneous, the chemical compositions of the glass in the starting material and run
163 products were estimated as the average of multiple point analyses of 19–35 spots with an

164 acceleration voltage of 15 kV, a beam current of 10 nA, and a probe diameter of 10 μm.
165 The weight fraction of spinel in the run products was calculated based on the mass balance
166 of MgO and Al_2O_3 between the bulk composition of the starting material and the
167 composition of the glass in the run products (Table 1). The obtained chemical
168 compositions of the glass in the run products were used to calculate the oxygen number
169 density, which was required to obtain the isotope exchange kinetics, using the calculated
170 melt density at the experimental temperatures based on Lesher and Spera (2015).
171 The oxygen isotope analysis of the glass in the run products and the starting
172 material was carried out using a secondary ion mass spectrometry (SIMS) (Cameca ims-
173 1280HR) at Hokkaido University. The analytical procedure of the SIMS is similar to that
174 described in Yamamoto et al. (2021). A $^{133}Cs^+$ primary beam (20 keV, 3 nA, and ~10 μm
175 in diameter) rastered over a 20 × 20 μm^2 area for 30 s was used for presputtering. The
176 raster size was then reduced to 2 × 2 μm^2 area for the data collection. Negative secondary
177 ions ($^{16}O^-$ and $^{18}O^-$) were collected simultaneously in multi-collection mode using two
178 Faraday cups (with feedback resisters of 10^{10} Ω for $^{16}O^-$ and 10^{11} Ω for $^{18}O^-$) for 10 s.
179 The magnetic field was controlled by an NMR probe. The mass resolution of $M/\Delta M$ was
180 set at ~2000. A normal incident electron flood gun was used for the electrostatic charge
181 compensation of the analyzed area during the measurements. The count rates were
182 corrected for the background and relative yield of each detector. For the correction of the
183 instrumental mass fractionation, Russian spinel ($\delta^{18}O$ = 8.5 ‰ relative to SMOW;
184 Yurimoto et al., 1994) was used as a standard. The reproducibility of the measured
185 $^{18}O/(^{16}O+^{18}O)$, determined by repetitive measurements (n = 20) of Russian spinel, was
186 typically 0.3–0.6‰ (2 standard deviations). The oxygen isotope profiles were obtained in
187 lines along one surface to the opposite surface, passing through the center of the spherical
188 sample at intervals of ~10–90 μm (typically 50 μm). The radius of each spherical sample
189 was determined from its diameter along the isotope profile (Table 2). After SIMS analysis,
190 the distances of the analytical SIMS craters from the sample surface and the absence of
191 spinel grains at each analytical point were observed using the FE-SEM.

3. RESULTS

3.1. Chemical composition and structure of run products

The run products are 2.6–2.8 mm-diameter spherical droplets, composed of chemically homogeneous glass and a small amount of spinel crystals with sizes of ≤ ~10 μm in diameter. No significant changes in size and elemental composition were observed after the experiments, but not in the oxygen isotope composition (see the next section). Spinel crystals both in the starting material and run products are heterogeneously distributed throughout the samples; they occur near the melt surface, along the wire loop, and at the top and bottom portion along the hanging direction, similar to those in the products by Yamamoto et al. (2021).

The difference between the starting material and the run products is the abundance of spinel crystals. The abundance of spinel increases from ~9 to ~12 wt% during heating at 1420°C (Table 1). This reflects crystallization of spinel towards its equilibrium abundance at 1420°C. The fraction of spinel crystallized during the oxygen isotope exchange experiments is at most ~3wt% (Table 1), which did not significantly change the melt composition and thus should not affect the kinetics of the oxygen isotope exchange reaction between the CAI melt and CO gas.

3.2. Oxygen isotope compositions

The profiles of the oxygen isotope compositions ($f^{18}O = {}^{18}O/({}^{16}O + {}^{18}O)$) of the glass in the samples heated at different P_{CO} and temperatures are shown in Figs. 1 and S1. The $f^{18}O$'s values of the glass show zoning profiles from the surface to the interior, where the $f^{18}O$ decreases toward the interior, and those at the surface and the center of the sample increase with time. This temporal change in zoning profiles suggests that the profiles were formed by the gas-melt isotope exchange at the surface and the diffusive transport of oxygen isotopes into the melt interior as observed in oxygen isotope exchange experiments between CAI melt and H_2O (Yamamoto et al., 2021).

We also found that the samples heated at a higher P_{CO} has a higher $f^{18}O$ at the surface and a steeper gradient in the zoning profile. The change in $f^{18}O$ at the surface in the present experiments is much smaller than that observed in the oxygen isotope exchange experiments between the CAI melt and H_2O (Yamamoto et al., 2021). This indicates a less effective oxygen isotope exchange reaction between the CAI melt and CO gas compared to that between the CAI melt and H_2O, as discussed below.

3.3. Gas species during the experiments

QMS spectra at 1420°C and 0.5 Pa of $C^{16}O$ and $C^{18}O$ gas (Fig. 2) show that the most dominant gas species were $C^{16}O^+$ (*m/z* = 28) and $C^{18}O^+$ (*m/z* = 30) in the experiments with $C^{16}O$ and $C^{18}O$ gas, respectively. The peaks at *m/z* = 16 ($^{16}O^+$) and 18 ($^{18}O^+$) partially originate from $C^{16}O$ and $C^{18}O$, respectively, due to CO cracking by electron impact ionization ($O^+/CO^+ \sim 0.01$; Ramanjaneyulu et al., 2014). The presence of cracked $^{18}O^+$ prevented us from measuring the partial pressure of $H_2{}^{16}O^+$ (*m/z* = 18) independently in experiments with $C^{18}O$.

We observed a prominent peak at *m/z* = 20 in the experiments with $C^{18}O$ gas (Fig. 2), which was not observed in the experiments with $C^{16}O$ gas. The most likely gas species at *m/z* = 20 was $H_2{}^{18}O$, which was present at a partial pressure of typically (1–0.3) × 10^{-4} Pa during the experiments (Fig. S2). The presence of $H_2{}^{18}O$ suggests that the $H_2{}^{18}O$ formation occurs at 1420°C through (1) isotope exchange between $C^{18}O$ gas and isotopically-normal H_2O gas that was present as residual gas in the system and/or (2) chemical reaction between $C^{18}O$ and H_2 provided from the CO gas cylinder. Both cases are plausible because (1) the oxygen isotope exchange between CO and H_2O gas should be rapid (Alexander, 2004; Lyons et al., 2009) and (2) $H_2{}^{18}O$ at pressures of 10^{-4}–10^{-5} Pa can be present at equilibrium in the system of CO : H_2 : N_2 ≈ 97.2 : 2.2 : 0.6 at 1420°C, calculated with FactSage 8.0 thermodynamic software package. It is not easy to determine the relative contributions of (1) and (2), but the presence of a small amount of $H_2{}^{18}O$ in

247 the system could affect the oxygen isotope exchange of the CAI analog melt, as discussed
248 below.
249
250 **4. DISCUSSION**
251 **4.1. Oxygen isotope exchange kinetics between CAI melt and gas**
252 A balance between the oxygen isotope exchange flux at the surface of the
253 CAI melt sphere and the oxygen diffusion flux into the interior gives;

254 $$k\left(f^{18}\mathrm{O}(a)-f^{18}\mathrm{O}_{\mathrm{gas}}\right)=-D\left(\partial f^{18}\mathrm{O}/\partial r\right)_{r=a}, \quad (1)$$

255 where k is the rate constant of the isotope exchange reaction at the melt surface, $f^{18}\mathrm{O}$ (a)
256 is $f^{18}\mathrm{O}$ at the surface (a represents the melt radius), $f^{18}\mathrm{O}_{\mathrm{gas}}$ is the oxygen isotope
257 composition of surrounding gases that exchanges oxygen isotopes with the CAI melt, D
258 is the diffusion coefficient of oxygen-bearing species in the melt, and r is the distance
259 from the spherical center of the melt (Crank, 1975; Yamamoto et al., 2021). The solution
260 of Eq. (1) can be expressed as follows:

261 $$\frac{f^{18}\mathrm{O}-f^{18}\mathrm{O}_{\mathrm{gas}}}{f^{18}\mathrm{O}_0-f^{18}\mathrm{O}_{\mathrm{gas}}}=\frac{2La}{r}\sum_{n=1}^{\infty}\frac{\exp\left(-D\beta_n{}^2t/a^2\right)}{\left\{\beta_n{}^2+L\left(L-1\right)\right\}}\frac{\sin\beta_n r/a}{\sin\beta_n}, \quad (2)$$

262 β_n the nth positive roots of the

263 $$\beta_n\cot\beta_n+L-1=0, \quad (3)$$

264 and L is a dimensionless variable expressed as follows:

265 $$L=ka/D, \quad (4)$$

266 where $f^{18}\mathrm{O}_0$ is the initial value of $f^{18}\mathrm{O}$, which is defined as the oxygen isotope
267 composition of the starting material (~0.0021), and t is the heating duration. The value of
268 the oxygen isotope composition of CO gas (98% $^{18}\mathrm{O}$) was applied for $f^{18}\mathrm{O}_{\mathrm{gas}}$ because the
269 experiments were conducted under the steady-state flow of CO gas and the amount of
270 oxygen isotopes exchanged with the CAI melt was not large enough to consider its effect
271 on the gas isotope composition.

Because H_2O gas is an effective oxygen isotope exchange partner for CAI melt (Yamamoto et al., 2021), the effect of a small amount of water vapor in the furnace (Fig. 2) should also be considered in the above discussion. It is reasonable to consider that the $f^{18}O$ of H_2O gas is equal to that of CO for both cases (1) (rapid isotope equilibrium between $C^{18}O$ and H_2O) and (2) (reaction between $C^{18}O$ and hydrogen) (section 3.3). The k in Eq. (1) represents the net surface isotope exchange rate, which is the sum of the exchange rates with CO (k_{CO}) and H_2O (k_{H2O}). For simplicity, we used a single diffusion coefficient D because the self-diffusion of oxygen (not H_2O) controlled the oxygen isotope transport inside the melt in our previous study (Yamamoto et al., 2021).

The fitting results of the obtained oxygen isotope profiles with Eq. (2) are shown in Figs. 1 and S1 and summarized in Table. 2. The D was evaluated only for the profiles obtained at P_{CO} = 0.5 and 1 Pa because the flat $f^{18}O$ profiles at P_{CO} = 0.1 Pa results in unreliable estimates of D and k. We thus used a weighted average of D evaluated at P_{CO} = 0.5 and 1 Pa was used to estimate k at P_{CO} = 0.1 Pa.

The obtained D's in the CAIB melt at 1420°C and 1460°C are almost constant in the range of (1–4) × 10^{-11} m^2 s^{-1} with an average value of (1.78 ± 0.16) × 10^{-11} m^2 s^{-1} (2 standard error) irrespective of the heating duration and P_{CO} (Table 2 and Fig. 3). The D in this study agrees well with D obtained through oxygen isotope exchange experiments between CAI melt and H_2O gas at 1420°C [(1.62 ± 0.15) × 10^{-11} m^2 s^{-1}; Yamamoto et al., 2021]. Because the contribution of $H_2{}^{18}O$ to the oxygen isotope profiles is much smaller than that of $C^{18}O$ in the present experiments as discussed below, this consistency suggests that the O^{2-} anion is the dominant diffusion species rather than molecular CO, H_2O, or other related ionic species (i.e., CO_3^{2-} and OH^-) (Zhang et al., 2007 and references therein). The obtained D is regarded as the oxygen self-diffusivity (D_{OX}) in the CAI melt, and the above assumption of a single D for the reactions with CO and H_2O is confirmed to be valid.

The QMS analysis showed that P_{H2O} was ~3–4 orders of magnitude smaller than P_{CO} during the experiments (Figs. 2 and S2). With a water vapor pressure of (1–0.3)

300 × 10^{-4} Pa with the same $f^{18}O$ as $C^{18}O$ gas, k is expressed as the combination of k for CO
301 gas (k_{CO}) and H_2O gas (k_{H2O}):

302 $$k_{net} = k_{CO} + k_{H_2O}. \quad (5)$$

303 The rate constant k_i (i = CO, H_2O) is expressed by:

304 $$k_i = \left(\alpha_i J_i\right) / C_O \quad (6)$$

305 where J_i is the flux of gas i, C_O is the oxygen number density of the melt, and α_i is a
306 dimensionless parameter representing the isotope exchange efficiency of the molecules
307 hitting the melt surface (Yamamoto et al., 2021). C_O was calculated with the theoretical
308 melt density based on Lesher and Spera (2015) and is typically ~4.4 × 10^{28} m^{-3} for the
309 melt in this study. The kinetic theory of gases gives J_i as:

310 $$J_i = \frac{P_i}{\sqrt{2\pi m_i k_B T}} \quad (7)$$

311 where P_i and m_i are the partial pressure and molecular weight of the gas i, respectively.
312 For both CO and H_2O gases, k in Eq. (5) is thus expressed as follows using Eq. (6):

313 $$k = \left(\alpha_{CO} J_{CO} + \alpha_{H_2O} J_{H_2O}\right) / C_O. \quad (8)$$

314 With α_{H2O} of 0.28 for the CAIB melt (Yamamoto et al., 2021), the contribution of H_2O to
315 oxygen isotope exchange with P_{H2O} of 3 × 10^{-5} and 1 × 10^{-4} Pa were calculated and
316 compared with the $f^{18}O$ profiles of the samples heated for the shortest and longest
317 durations in the present experiments (Figs. 4 and S3). This represents the experimental
318 $f^{18}O$ profiles that show much greater ^{18}O enrichment than the calculated profiles for
319 isotope exchange with $H_2{}^{18}O$. This suggests that the exchange with $C^{18}O$ is clearly
320 required to explain the obtained $f^{18}O$ profiles and that k is mainly determined by k_{CO}.
321 By taking the contribution of H_2O into account for P_{H2O} of 3 × 10^{-5} and 1 ×
322 10^{-4} Pa, α_{CO} was estimated from the obtained k based on Eq. (8) (Fig. 5; Table 2).
323 Although the value of P_{H2O} gives an additional uncertainty for the estimate of α_{CO}, we

found that the values of α_{CO} are on the orders of 10^{-3}–10^{-4}, which is 2–3 orders of magnitude smaller than that of α_{H2O} (~0.28; Yamamoto et al., 2021). The partial pressure of $H_2{}^{18}O$ rapidly decreased down to ~3–6 × 10^{-5} Pa within 1 h after the sample temperature reached its maximum (Fig. S2), and the samples were heated for more than ~1 h in 14 out of 16 experiments (Tables 1 and 2). Therefore, we estimated α_{CO} to be (3.8 ± 0.7) × 10^{-4} and (3.1 ± 0.4) × 10^{-4} at P_{H2O} of 3 × 10^{-5} and 6 × 10^{-5} Pa, respectively, and adopted an average value of (3.3 ± 0.6) × 10^{-4} as a more plausible value of α_{CO}.

The dimensionless parameter L is related to the relative rates of the surface reaction and diffusion in the melt [Eq. (4)] (e.g., Tsuchiyama et al., 1999; Richter , 2004; Yamamoto et al., 2021). When the rate of diffusive transport of isotopes is faster than the surface isotope exchange rate, L becomes smaller than ~1. On the other hand, L becomes larger than ~1 when the surface isotope exchange rate is faster than the rate of diffusive transport. The obtained L (= $ka/D \approx k_{CO}a/D$) (Eqs. 4 and 5) in this study are on the orders of 10^{-2}–10^{-3} (Table 2; Fig. 6). This small L suggests that the overall isotope exchange rate is controlled by the isotope exchange process at the melt surface, with a smaller contribution of diffusive transport that forms the $f^{18}O$ profiles in this study (Figs. 1 and S1). The values of L increase with increasing P_{CO}, resulting in a steeper concentration gradient in the melt at higher P_{CO} (Table 2; Figs. 1, S1, and 6).

We finally discuss the oxygen self-diffusion coefficient in the CAI melt. The D_{OX} in this study is similar to those determined for dry basaltic melt, which has a similar degree of melt polymerization (NBO/T; non-bridging oxygen/tetrahedrally coordinated cation) of ~1 as that of the CAIB melt (NBO/T ~1.1), at 1420°C (2.12–2.52 × 10^{-11} m^2 s^{-1}) (Canil and Muehlenbachs, 1990; Lesher et al., 1996) because the self-diffusion of oxygen in dry silicate melts depends on NBO/T (Liang et al., 1996; Zhang and Ni, 2010). Liang et al. (1996) parameterized the dependence of the self-diffusivity of oxygen in dry silicate melts on the viscosity (η) as follows:

$$D_{OX} = \left(33.080\eta^{-0.722}\right) \times 10^{-12} \left(\mathrm{m^2\ s^{-1}}\right) \quad (9)$$

Given a viscosity at 1420°C for the CAIB melt calculated with a FactSage 8.0

thermodynamic software package (0.83 Pa s) and that estimated from a measured viscosity of a melt with a composition of 8MgO-28Al_2O_3-32SiO_2-32CaO (wt%) (Mishra et al., 1994) similar to the glass composition of the starting material (Table 1) (1.46 Pa s), D_{OX}'s are estimated to be 3.8 × 10^{-11} m^2 s^{-1} and 2.5 × 10^{-11} m^2 s^{-1}, respectively. These estimated D_{OX}'s are consistent with the range of D_{OX}'s estimated in this study (Table 2). When the above relation is applied for D_{OX}'s of CAI melts with a range of chemical compositions, D_{OX} for compositions CAIδ and CAIϕ (Grossman et al., 2002) are 4.2 × 10^{-11} and 3.8 × 10^{-11} m^2 s^{-1}, respectively. Both CAI δ and CAIϕ are the compositions of CAI precursors along the equilibrium condensation sequence (Grossman et al., 2002), and their viscosities at 1420°C were estimated using the FactSage software considering the equilibrium amounts of spinel. This calculation result suggests that D_{OX} does not vary significantly with the chemical composition of CAI melt at the same temperature. We also note that D_{OX} at 1420 and 1460°C are not large enough to observe the difference in D_{OX} beyond the experimental uncertainty (Fig. 3). When the activation energy for self-diffusion coefficient of oxygen in the basaltic melt (~170 kJ mol^{-1}; Lesher et al., 1996) is assumed (Yamamoto et al., 2021), D_{OX} at 1460 °C is only 1.3 times larger than that at 1420°C, and this difference is smaller than the degree of scattering in the D_{OX} values (Fig. 3).

We thus conclude that D_{OX} of a few × 10^{-11} m^2 s^{-1} can be applied to type B CAI melts at the temperatures above their melilite liquidus.

4.2 Application to the thermal histories of igneous CAIs

Here we discuss the oxygen isotope exchange of igneous CAIs in the solar composition disk gas based on the oxygen isotope exchange kinetics between CAI and CO (this study), CAI and H_2O (Yamamoto et al.,2021), and CO and H_2O (Alexander, 2004).

The degree of oxygen isotope exchange of a melt sphere for a given heating duration t can be calculated as follows (Crank, 1975; Yamamoto et al., 2021):

$$x = 1 - \sum_{n=1}^{\infty} \frac{6L^2 \exp\left(-\beta_n{}^2 Dt / a^2\right)}{\beta_n{}^2 \left\{\beta_n{}^2 + L\left(L-1\right)\right\}} \quad (10)$$

where x is the degree of oxygen isotope exchange of the bulk sphere toward isotope equilibrium ($x = 1$). We first determine the timescales required for $x = 0.9$ through oxygen isotope exchange reaction between a CAI melt sphere and CO with α_{CO} of 3.3×10^{-4} as a function of P_{CO} at 1420°C (Fig. 7). The size of melt sphere is assumed to be 1 cm in diameter, a typical size of natural type B CAIs (MacPherson and Grossman, 1981; Podosek et al., 1991; Simon and Grossman, 2006; Bullock et al., 2013; Kawasaki et al., 2018). The L in Eq. (10) for a given P_{CO} was obtained by Eqs. (4), (6), and (7), and β_n was calculated by the obtained L for a given P_{CO} using Eq. (3). The timescale required for $x = 0.9$ by the isotope exchange reaction between the CAI melt and H_2O is also shown in Fig. 7 (Yamamoto et al., 2021). We note that the redox condition is considered to be close to that of the solar composition based on the redox state of Ti in fassaite in natural type B CAIs (Grossman, 2008), and the horizontal axis in Fig. 7 is expressed as P_{H2} considering the solar composition P_{H2O}/P_{H2} and P_{CO}/P_{H2} ratios of 10^{-3} (Wood and Hashimoto, 1993; Lodders, 2021).

The timescale of isotope exchange between CAI and CO gas depends almost linearly on P_{H2} in the range of P_{H2} shown in Fig. 7 because the supply of CO gas to the melt controls the rate of overall isotope exchange reaction (Yamamoto et al., 2018, 2020). On the other hand, the timescale for isotope exchange between the CAI melt and H_2O becomes almost constant at $P_{H2} > \sim 10^3$ Pa because the effect of oxygen isotope diffusion in the melt becomes prominent at higher pressures owing to the rapid surface isotope exchange rate of the CAI melt with H_2O compared with CO gas.

The timescale of the isotope exchange between H_2O and CO is determined by P_{H2O} (Alexander, 2004, Lyons et al., 2009) and is shown in Fig. 7. The timescale for the H_2O-CO reaction is always shorter than those of isotope exchange between the CAI melt and H_2O or CO. Therefore, H_2O and CO had the same oxygen isotope composition during the reheating events of CAIs, and both H_2O and CO contributed to the oxygen

isotope evolution of CAIs in the same direction. In this case, the oxygen isotope exchange timescale between the CAI melt and H_2O/CO gas is dominated by the isotope exchange reaction with H_2O gas that can exchange oxygen isotopes with the melt effectively. Therefore, even if the effect of CO gas is taken into account, the heating timescale of the CAI melt should thus be at least 2–3 days (Fig. 7; Yamamoto et al., 2021) to explain the homogeneous ^{16}O-poor isotope compositions of melilite in typical igneous CAIs, including type B CAIs (McKeegan et al., 1996; Yurimoto et al., 2008 and references therein; Aléon, 2016; Kawasaki et al., 2018).

Connolly and Burnett (2003) conducted isothermal experiments at 1450°C for 3, 30, and 90 h in the CAI melt-spinel system and found that the concentrations of V and Ti in spinel became completely equilibrated with the co-existing melt through diffusion for 90 h, which is inconsistent with the inhomogeneous concentration of these minor elements in spinel of natural CAIs (Connolly et al., 2003). They concluded that heating at the maximum temperature should be less than ~100 h for natural igneous CAIs. This maximum heating duration of 100 h is close to the minimum heating timescale proposed in this study (2–3 days).

Oxygen self-diffusion coefficients in spinel (Ryerson and McKeegan, 1994) suggest that little diffusion of oxygen (<< 1μm) occurs from the melt to spinel during 2–3 day-heating at ~1400°C (Fig. 7). This indicates that spinel grains could maintain their original oxygen isotope composition during the remelting events, which is consistent with the oxygen isotope analysis of CAIs with high spatial resolution (Yurimoto et al., 2003; Suzumura et al., 2021).

A P_{H2} higher than ~100 Pa (i.e., $P_{H2O} > 0.1$ Pa) is required for the heating timescale of 2–3 days during the type B CAI formation (Fig. 7), suggesting that type B CAIs were heated at the maximum temperature of ~1400°C for ~2–3 days under $P_{H2} >$ 100 Pa.

5. Conclusions

We determined oxygen isotope exchange kinetics between type B CAI-like melt and low-pressure CO gas through experiments conducted at 1420°C and 1460°C (above the melilite liquidus) under ^{18}O-enriched CO gas pressures of 0.1, 0.5, and 1 Pa. All the samples show the enrichment of ^{18}O at the surface and have oxygen isotope zoning toward the interior. The zoning profiles were well-fitted with a three-dimensional spherical diffusion model with changing the surface ^{18}O concentration due to the gas-melt surface reaction. The obtained diffusion coefficient of 1.8×10^{-11} m^2 s^{-1} agrees well with that obtained in the isotope exchange experiments between the CAI melt and H_2O gas, suggesting that the O^{2-} anion is the dominant diffusion species. The estimated surface oxygen isotope exchange efficiencies of $\sim 3 \times 10^{-4}$ for colliding CO molecules are ~~3~~ three orders of magnitude smaller than that for H_2O molecules, which indicates a much smaller isotope exchange rate of the CAI melt with CO gas compared with that with H_2O gas.

In the CAI melt-CO-H_2O system, the order of isotope exchange rates (k) always obeys the relation of $k_{CO\text{-}H2O} > k_{CAI\ melt\text{-}H2O} \geq k_{CAI\ melt\text{-}CO}$, and the oxygen isotope exchange rate between the CAI melt and disk gas is controlled by the reaction between the CAI melt and H_2O gas. This timescale comparison suggests that the typical type B CAIs with the homogeneous oxygen isotope composition of melilite are likely to be heated for 2–3 days at P_{H2} greater than 100 Pa above the melilite liquidus.

Acknowledgments

The authors thank S. A. Whattam and an anonymous reviewer for their constructive reviews and comments, which improved this paper. The authors are grateful to T. Mikouchi for granting permission to use the one-atmosphere furnace to synthesize the CAI analogs. N. K. thanks N. Sakamoto for technical support in the SIMS analysis. The authors are also grateful to H. Yoshida for the EPMA analysis. This work was financially supported by the Ministry of Education, Sports, Science and Technology KAKENHI grants.

Appendix. Supplementary material

Supplementary data associated with this article can be found in the online version.

References

Aléon J., Goresy A. E., and Zinner E. (2007) Oxygen isotope heterogeneity in the earliest protosolar gas recorded in a meteoritic calcium-aluminum-rich inclusion. *Earth Plane. Sci. Lett.* 263, 114–127.

Aléon J. (2016) Oxygen isotopes in the early protoplanetary disk inferred from pyroxene in a classical type B CAI. *Earth Plane. Sci. Lett.* 440, 62–70.

Alexander C. M. O'D. (2004) Chemical equilibrium and kinetics constrains for chondrule and CAI formation conditions. *Geochim. Cosmochim. Acta* 68, 3943–3969.

Amelin Y., Krot A. N., Hutcheon I. D. and Ulyanov A. A. (2002) Lead isotopic ages of chondrules and calcium-aluminum-rich inclusions. *Science* 297, 1678–1683.

Bullock E. S., Knight K. B., Richter F. M., Kita N. T., Ushikubo T., MacPherson G. J., Davis A. M. and Mendybaev A. M. (2013) Mg and Si isotope fractionation patterns in types B1 and B2 CAIs: Implications for formation under different nebular conditions. *Meteorit. Planet. Sci.* 48, Nr 8, 1440–1458.

Canil D. and Muehlenbachs K. (1990) Oxygen diffusion in an Fe-rich basalt melt. *Geochim. Cosmochim. Acta* 5, 2947–2951.

Clayton R. N., Onuma N., Grossman L. and Mayeda T. K. (1977) Distribution of the pre-solar component in Allende and other carbonaceous chondrites. *Earth Planet. Sci. Lett.* 34, 209–224.

Clayton R. N. (1993) Oxygen isotopes in meteorites. *Annu. Rev. of Earth Planet. Sci.* 21, 115–149.

Connolly H. C. Jr. and Burnett D. S. (2003) On type B CAI formation: Experimental constraints on fO_2 variations in spinel minor element partitioning and reequilibration effects. *Geochim. Cosmochim. Acta* 67, 4429–4434.

Connelly J. N., Bizzarro M., Krot A. N., Nordlund Å., Wielandt D. and Ivanova M. A. (2012) The absolute chronology and thermal processing of solids in the solar protoplanetary disk. *Science* 338, 651–655.

Crank J. (1975) *The Mathematics of Diffusion*, 2nd edition, Clarendon Press, Oxford.

Grossman L. (1972) Condensation in the primitive solar nebula. *Geochim. Cosmcochim. Acta* 36, 597–619.

Grossman L., Ebel D. S., and Simon S. B. (2002) Formation of refractory inclusions by evaporation of condensate precursors. *Geochim. Cosmochim. Acta* 66, 145–161.

Grossman L., Beckett J. R., Fedkin A.V., Simon S. B. and Ciesla F. J. (2008) Redox conditions in the Solar Nebula: Observational, Experimental, and Theoretical Constraints. In *Reviews in Mineralogy and Geochemistry* (eds. MacPherson G. J.). vol. 68. Mineralogical Society of America, Washington, D.C., pp. 93–140.

Ito M., Nagasawa H. and Yurimoto H. (2004) Oxygen isotopic SIMS analysis in Allende CAI: Details of the very early thermal history of the solar system. *Geochim. Cosmochim. Acta* 68, 2905–2923.

Kamibayashi M., Tachibana S., Yamamoto D., Kawasaki N., and Yurimoto H. (2021) Effect of hydrogen gas pressure on calcium-aluminum-rich inclusion formation in the protoplanetary disk: A Laboratory simulation of open-system melt crystallization. *Astrophy. J. Letters* 923, L12(8pp).

Kawasaki N., Kato C., Itoh S., Wakaki S., Ito M. and Yurimoto H (2015) ^{26}Al–^{26}Mg chronology and oxygen isotope distributions of multiple melting for a Type C CAI from Allende. *Geochim. Cosmochim. Acta* 169, 99–114.

Kawasaki N., Simon S. B., Grossman L., Sakamoto N. and Yurimoto H. (2018) Crystal growth and disequilibrium distribution of oxygen isotopes in an igneous CA-Al-rich inclusion from the Allende carbonaceous chondrite. *Geochim. Cosmochim. Acta* 221, 318–341.

Kawasaki N., Wada S., Park C., Sakamoto N. and Yurimoto H (2020) Variations in initial ^{26}Al/^{27}Al ratios among fine-grained Ca-Al-rich inclusions from reduced CV chondrites. *Geochim. Cosmochim. Acta* 279, 1–15.

Kawasaki N., Itoh S, Sakamoto N., Simon S. B., Yamamoto D. and Yurimoto H. (2021) Oxygen and Al-Mg isotopic constraints on cooling rate and age of partial melting of an Allende Type B CAI, Golfball. *Meteorit. Planet. Sci.* 56, 1224–1239.

Lesher C. E., Hervig R. L. and Tinker D. (1996) Self-diffusion of network formers (silicon and oxygen) in naturally occurring basaltic liquid. *Geochim. Cosmochim. Acta* 60, 405–413.

Lesher C. E. and Spera F. J. (2015) Thermodynamics and transport properties of silicate melts and magma. In *The encyclopedia of volcanoes* (eds. Sigurdsson, H.), 2nd Edition, Academic Press, Amsterdam, pp. 113–141.

Liang Y., Richter F. M., Davis A. M. and Watson E. B. (1996) Diffusion in silicate melts: I. Self diffusion in CaO-Al_2O_3-SiO_2 at 1500°C and 1 GPa. *Geochim. Cosmochim. Acta* 60, 4353–4367.

Lodders K. (2021) Relative atomic solar system abundances, mass fractions, and atomic masses of the elements and their isotopes, composition of the solar photosphere, and compositions of the major chondritic meteorite groups. *Space Science Review* 217, 44.

Lyons J. R. and Young E. D. (2005) CO self-shielding as the origin of oxygen isotpe anomalies in the early solar nebula. Nature 435, 317–320.

Lyons J. R., Bergin E. A., Ciesla F. J., Davis A. M., Desch S. J., Hashizume L. and Lee J.-E. (2009) Timescales for the evolution of oxygen isotope compositions in the solar nebula. *Geochim. Cosmochim. Acta* 73, 4998–5017..

MacPherson G. J. and Grossman L. (1981) A once-molten, coarse-grained, Ca-rich inclusion in Allende. *Earth Planet. Sci. Lett*. 52, 16–24.

MacPherson G. J., Paque J. M., Stolper E. and Grossman L. (1984) The origin and significance of reverse zoning in melilite from Allende type B inclusions. *J. Geol.* 92, 289–305.

MacPherson G. J. (2014) Calcium-aluminum-rich inclusions in chondritic meteorites. In *Meteorites and Cosmochemical Processes* (eds. Davis A. M). *Treatise on Geochemistry*, vol. 1. Elsevier-Pergamon, Oxford, pp. 139–179.

McKeegan K. D., Leshin L. A., Russell S. S. and MacPherson G. J. (1996) *In situ* measurement of O isotopic anomalies in a Type B Allende CAI. *Meteorit. Planet. Sci.* 31, A86–A87.

Mendybaev R. A., Richter F. M. and Davis A. M. (2006) Crystallization of melilite from CMAS-liquids and the formation of melilite mantle of Type B1 CAIs: Experimental simulations. *Geochim. Cosmochim. Acta* 70, 2622–2642.

Mishra U. N., Thakur B., and Thakur M. N. (1994) Investigation on viscosity of very high alumina slags for blast furnace. *SEAISI Q* 23, 72–82.

Ramanjaneyulu P. S., Chandra K., Kulkarni A. S., Yadav C. S., Saha A., Saxena M. K., Tomar B. S., and Ramakumar K. L. (2014) Determination of total gas content and its composition in Indian PFBR blanket pellets. J. Radioanal. Nucl. Chem. 301, 117–124.

Richter F. M. (2004) Timescales determining the degree of kinetic isotope fractionation by evaporation and condensation. *Geochem. Cosmochim. Acta* 68, 4971–4992.

Podosek F. A., Zinner E. K., MacPherson G. J., Lundberg L. L., Brannon J. C. and Fahey A. J. (1991) Correlated study of initial $^{87}Sr/^{86}Sr$ and Al-Mg isotopic systematics and petrologic properties in a suite of refractory inclusions from the Allende meteorite. *Geochem. Cosmochim. Acta* 55, 1083–1110.

Ryerson F. J. and McKeegan K. D. (1994) Determination of oxygen self-diffusion in åkermanite, anorthite, diopside, and spinel: Implications for oxygen isotopic anomalies and the thermal history of Ca-Al-rich inclusions. *Geochim. Cosmochim. Acta* 58, 3713–3734.

Simon S. B. and Grossman L. (2006) A comparative study of melilite and fassaite in Type B1 and B2 refractory inclusions. *Geochim. Cosmochim. Acta* 70, 780–798.

Stolper E. (1982) Crystallization sequences of Ca-Al-rich inclusions from Allende: An experimental study. *Geochim. Cosmochim. Acta* 46, 2159–2180.

Stolper E. and Paque J. M. (1986) Crystallization sequences of Ca-Al-rich inclusions from Allende: The effects of cooling rate and maximum temperature. *Geochim. Cosmochim. Acta* 50, 1785–1806.

Suzumura A., Kawasaki N., Seto Y., Yurimoto H. and Itoh S. (2021) Origin of minerals in åkermanite-rich patch texture and oxygen isotopic evolution of compact Type A Ca-Al-rich inclusions from the Northwest Africa 7865 CV chondrite. *Geochim.*

Cosmochim. Acta 303, 51–65.

Tsuchiyama A., Tachibana S. and Takahashi T. (1999) Evaporation of forsterite in the primordial solar nebula; rates and accompanied isotope fractionation. *Geochim. Cosmochim. Acta* 63, 2451–2466.

Wark D. (1979) Birth of the presolar nebula: The sequence of condensation revealed in the Allende meteorite. *Astrophys. Space Sci.* 65, 275–295.

Wood J. A. and Hashimoto A. (1993) Mineral equilibrium in fractionated nebular systems. *Geochim. Cosmochim. Acta* 57, 2377–2388.

Yamamoto D., Kuroda M., Tachibana S., Sakamoto N. and Yurimoto H. (2018) Oxygen isotope exchange between amorphous silicate and water vapor and its implications for oxygen isotope evolution in the early Solar System. *Astrophy. J.* 865, 98 (14pp).

Yamamoto D., Tachibana S., Kawasaki N. and Yurimoto H. (2020) Survivability of presolar isotopic signatures of amorphous silicate dust in the protosolar disk. *Meteoritic. Planet. Sci.* 55, 1281–1292.

Yamamoto D., Kawasaki N., Tachibana S., Kamibayashi M., and Yurimoto H. (2021) An experimental study on oxygen isotope exchange reaction between CAI melt and low-pressure water vapor under simulated Solar nebula conditions. *Geochimi. Cosmochim. Acta* 314,108–120.

Yoshitake M., Koide Y. and Yurimoto H. (2005) Correlations between oxygen-isotopic composition and petrologic setting in a coarse-grained Ca, Al-rich inclusion. *Geochimi. Cosmochim. Acta* 69, 2663–2674.

Yurimoto H., Nagasawa H, Mori Y. and Matsubayashi O. (1994) Micro-distribution of oxygen isotopes in a refractory inclusion from the Allende meteorite. *Earth planet Sci. Lett.* 128, 47–53.

Yurimoto H., Ito M. and Nagasawa H. (1998) Oxygen isotope exchange between refractory inclusion in Allende and solar nebula gas. *Science* 282, 1874–1877.

Yurimoto H., Nagashima K. and Kunihiro T. (2003) High precision isotope micro-imaging of materials. *Appl. Surf. Sci.* 203–204, 793–797.

Yurimoto H. and Kuramoto K. (2004) Molecular cloud origin for the oxygen isotope heterogeneity in the Solar System. *Science* 305, 1763–1766.

Yurimoto H., Krot A. N., Choi B-G., Aléon J., Kunihiro T. and Brearley A. J. (2008) Oxygen isotopes of chondritic components. In *Oxygen in the Solar System* (eds MacPherson G. J.). *Reviews in Mineralogy and Geochemistry*, vol. 68. Washington D.C.: Mineralogical Society of America. pp. 141–186.

Zhang Y., Xu Z., Zhu M., and Wang H. (2007) Silicate melt properties and volcanic eruptions. *Reviews of Geophysics* 45, RG4004.

Zhang Y. and Ni H. (2010) Diffusion of H, C, and O components in silicate melts. *Reviews in Mineralogy and Geochemistry* 72, 171–225.

Table 1. Experimental conditions and sample description.

Temp. (°C)	P_{CO} (Pa)	Duration (h)	Initial weight (mg)[a]	Glass composition (wt%)[a]							Spinel (wt%)[c]
				No. of analysis[b]	MgO	Al_2O_3	SiO_2	CaO	TiO_2	Total	
/	/	0[d]	/	25	8.3 ± 0.1[e]	24.2 ± 0.1	34.5 ± 0.1	31.6 ± 0.2	1.19 ± 0.02	99.8 ± 0.3	8.8 ± 0.2
1420	0.1	2	29.6	35	7.9 ± 0.1	23.6 ± 0.1	34.9 ± 0.1	32.2 ± 0.2	1.19 ± 0.02	99.7 ± 0.2	10.4 ± 0.2
		5	26.8	30	7.8 ± 0.1	24.3 ± 0.1	34.2 ± 0.1	31.8± 0.2	1.18 ± 0.02	99.3 ± 0.3	9.9 ± 0.3
		17	27.9	35	7.4 ± 0.1	25.1 ± 0.2	33.8 ± 0.1	32.4± 0.2	1.21 ± 0.02	99.9 ± 0.3	10.1 ± 0.3
		22	30.3	20	7.2 ± 0.1	24.5 ± 0.2	34.3 ± 0.1	32.4± 0.2	1.31 ± 0.03	99.7 ± 0.3	10.9 ± 0.3
1420	0.5	2	29.6	20	7.7 ± 0.2	23.6 ± 0.2	34.9 ± 0.1	32.2 ± 0.2	1.31 ± 0.02	99.8 ± 0.3	10.8 ± 0.4
		4	31.1	20	7.5 ± 0.1	23.8 ± 0.1	34.6 ± 0.2	32.3 ± 0.2	1.29 ± 0.02	99.4 ± 0.3	11.2 ± 0.3
		6	30.9	20	7.2 ± 0.1	23.4 ± 0.1	34.9 ± 0.1	32.8 ± 0.1	1.29 ± 0.03	99.7 ± 0.2	12.0 ± 0.4
		7	30.7	20	7.3 ± 0.2	24.0 ± 0.2	34.7 ± 0.2	32.6 ± 0.2	1.28 ± 0.03	99.8 ± 0.4	11.3 ± 0.4
		8	32.5	20	7.2 ± 0.1	23.8 ± 0.1	34.6 ± 0.2	32.5 ± 0.2	1.30 ± 0.03	99.4 ± 0.3	11.7 ± 0.3
		14	29.7	20	6.7 ± 0.1	24.5 ± 0.1	34.3 ± 0.2	32.8 ± 0.2	1.30 ± 0.03	99.6 ± 0.3	11.9 ± 0.3
1460	0.5	0.87	29.1	20	8.3 ± 0.1	24.5 ± 0.2	34.1 ± 0.2	31.3 ± 0.1	1.26 ± 0.02	99.5 ± 0.3	8.6 ± 0.3
		3	32.1	20	7.8 ± 0.1	24.5 ± 0.1	34.2 ± 0.1	31.8 ± 0.2	1.27 ± 0.02	99.6 ± 0.3	9.6 ± 0.3
		5	31.0	20	7.6 ± 0.2	24.8 ± 0.1	33.9 ± 0.1	32.0 ± 0.2	1.29 ± 0.02	99.5 ± 0.3	9.9 ± 0.4
1420	1	1	31.3	19	7.6 ± 0.2	23.3 ± 0.1	34.9 ± 0.2	32.2 ± 0.2	1.29 ± 0.03	99.3 ± 0.3	11.2 ± 0.4
		2.5	30.0	23	7.5 ± 0.1	23.3 ± 0.2	34.6 ± 0.1	32.4 ± 0.3	1.28 ± 0.03	99.1 ± 0.4	11.5 ± 0.4
		4	29.8	20	7.4 ± 0.1	24.0 ± 0.2	34.4 ± 0.2	32.3 ± 0.2	1.27 ± 0.03	99.5 ± 0.3	11.0 ± 0.3

[a]Average of multiple measurements of sample weight after subtracting the pre-determined weight of the platinum wire loop.

[b]Number of EPMA analysis spot.

[c]Estimated using the calculation method of melt density based on Lesher and Spera (2015) for each chemical composition of glass.

[d]Starting material used for the oxygen isotope exchange experiments.

[e]All the errors represent 2-sigma standard error.

Table 2. Self-diffusion coefficient of oxygen (D), net surface isotopic exchange rate (k), dimensionless parameter (L), and isotopic exchange efficiency of colliding CO gas molecules at the melt surface (α_{CO}).

Temp. (°C)	P_{CO} (Pa)	Duration (h)	Radius (mm)[a]	Profile ID[b]	D (m^2 sec^{-1})	k (m sec^{-1})	$L = k\,a/D$	α_{CO} ($P_{H2O} = 1 \times 10^{-4}$ (Pa))[c]	α_{CO} ($P_{H2O} = 3 \times 10^{-5}$ (Pa))[c]
1420	0.1	2	1.37	1	$\equiv 1.78 \times 10^{-11}$[d]	$(1.68 \pm 0.001) \times 10^{-11}$ [e]	$(1.29 \pm 0.001) \times 10^{-3}$	$(2.92 \pm 0.13) \times 10^{-4}$	$(5.28 \pm 0.04) \times 10^{-4}$
		2	1.37	2	$\equiv 1.78 \times 10^{-11}$	$(3.32 \pm 0.001) \times 10^{-11}$	$(2.56 \pm 0.001) \times 10^{-3}$	$(9.06 \pm 0.13) \times 10^{-4}$	$(1.14 \pm 0.004) \times 10^{-3}$
		5	1.31	1	$\equiv 1.78 \times 10^{-11}$	$(2.28 \pm 0.007) \times 10^{-11}$	$(1.67 \pm 0.005) \times 10^{-3}$	$(5.13 \pm 0.13) \times 10^{-4}$	$(7.49 \pm 0.05) \times 10^{-4}$
		5	1.31	2	$\equiv 1.78 \times 10^{-11}$	$(1.26 \pm 0.001) \times 10^{-11}$	$(9.29 \pm 0.004) \times 10^{-4}$	$(1.35 \pm 0.13) \times 10^{-4}$	$(3.71 \pm 0.04) \times 10^{-4}$
		17	1.27	1	$\equiv 1.78 \times 10^{-11}$	$(1.25 \pm 0.0002) \times 10^{-11}$	$(8.90 \pm 0.001) \times 10^{-4}$	$(1.31 \pm 0.13) \times 10^{-4}$	$(3.66 \pm 0.04) \times 10^{-4}$
		17	1.27	2	$\equiv 1.78 \times 10^{-11}$	$(2.40 \pm 0.006) \times 10^{-11}$	$(1.71 \pm 0.004) \times 10^{-3}$	$(5.64 \pm 0.13) \times 10^{-4}$	$(7.99 \pm 0.05) \times 10^{-4}$
		22	1.35	1	$\equiv 1.78 \times 10^{-11}$	$(1.18 \pm 0.001) \times 10^{-11}$	$(8.94 \pm 0.007) \times 10^{-4}$	$(1.04 \pm 0.13) \times 10^{-4}$	$(3.40 \pm 0.04) \times 10^{-4}$
		22	1.35	2	$\equiv 1.78 \times 10^{-11}$	$(2.15 \pm 0.004) \times 10^{-11}$	$(1.63 \pm 0.003) \times 10^{-3}$	$(4.69 \pm 0.13) \times 10^{-4}$	$(7.05 \pm 0.04) \times 10^{-4}$
1420	0.5	2	1.32	1	$(1.54 \pm 0.05) \times 10^{-11}$	$(3.30 \pm 0.12) \times 10^{-11}$	$(2.83 \pm 0.14) \times 10^{-3}$	$(1.80 \pm 0.10) \times 10^{-4}$	$(2.27 \pm 0.09) \times 10^{-4}$
		2	1.32	2	$(2.18 \pm 0.04) \times 10^{-11}$	$(3.32 \pm 0.16) \times 10^{-11}$	$(2.83 \pm 0.11) \times 10^{-3}$	$(1.81 \pm 0.12) \times 10^{-4}$	$(2.28 \pm 0.12) \times 10^{-4}$
		4	1.34	1	$(2.16 \pm 0.01) \times 10^{-11}$	$(5.26 \pm 0.11) \times 10^{-11}$	$(3.26 \pm 0.07) \times 10^{-3}$	$(3.25 \pm 0.09) \times 10^{-4}$	$(3.73 \pm 0.08) \times 10^{-4}$
		4	1.34	2	$(2.18 \pm 0.04) \times 10^{-11}$	$(5.61 \pm 0.07) \times 10^{-11}$	$(3.44 \pm 0.08) \times 10^{-3}$	$(3.51 \pm 0.06) \times 10^{-4}$	$(3.99 \pm 0.05) \times 10^{-4}$
		6	1.35	1	$(1.38 \pm 0.05) \times 10^{-11}$	$(4.33 \pm 0.10) \times 10^{-11}$	$(4.22 \pm 0.19) \times 10^{-3}$	$(2.56 \pm 0.08) \times 10^{-4}$	$(3.03 \pm 0.07) \times 10^{-4}$
		6	1.35	2	$(1.38 \pm 0.08) \times 10^{-11}$	$(4.30 \pm 0.15) \times 10^{-11}$	$(4.20 \pm 0.29) \times 10^{-3}$	$(2.53 \pm 0.11) \times 10^{-4}$	$(3.01 \pm 0.11) \times 10^{-4}$
		7	1.32	1	$(1.85 \pm 0.02) \times 10^{-11}$	$(4.29 \pm 0.12) \times 10^{-11}$	$(3.06 \pm 0.09) \times 10^{-3}$	$(2.54 \pm 0.10) \times 10^{-4}$	$(3.01 \pm 0.09) \times 10^{-4}$
		7	1.32	2	$(1.12 \pm 0.03) \times 10^{-11}$	$(4.21 \pm 0.02) \times 10^{-11}$	$(4.98 \pm 0.12) \times 10^{-3}$	$(2.48 \pm 0.03) \times 10^{-4}$	$(2.95 \pm 0.02) \times 10^{-4}$
		8	1.37	1	$(1.32 \pm 0.05) \times 10^{-11}$	$(4.36 \pm 0.08) \times 10^{-11}$	$(4.50 \pm 0.19) \times 10^{-3}$	$(2.57 \pm 0.06) \times 10^{-4}$	$(3.05 \pm 0.06) \times 10^{-4}$
		8	1.37	2	$(1.77 \pm 0.06) \times 10^{-11}$	$(4.67 \pm 0.03) \times 10^{-11}$	$(3.60 \pm 0.13) \times 10^{-3}$	$(2.81 \pm 0.04) \times 10^{-4}$	$(3.28 \pm 0.03) \times 10^{-4}$
		14	1.31	1	$(1.68 \pm 0.13) \times 10^{-11}$	$(4.93 \pm 0.09) \times 10^{-11}$	$(3.83 \pm 0.30) \times 10^{-3}$	$(3.01 \pm 0.07) \times 10^{-4}$	$(3.48 \pm 0.06) \times 10^{-4}$
		14	1.31	2	$(1.68 \pm 0.05) \times 10^{-11}$	$(4.93 \pm 0.04) \times 10^{-11}$	$(3.85 \pm 0.13) \times 10^{-3}$	$(3.01 \pm 0.304) \times 10^{-4}$	$(3.48 \pm 0.03) \times 10^{-4}$
1460	0.5	0.87	1.42	1	$(1.82 \pm 0.05) \times 10^{-11}$	$(7.58 \pm 0.22) \times 10^{-11}$	$(5.91 \pm 0.23) \times 10^{-3}$	$(5.05 \pm 0.17) \times 10^{-4}$	$(5.52 \pm 0.17) \times 10^{-4}$
		0.87	1.42	2	$(2.01 \pm 0.08) \times 10^{-11}$	$(8.42 \pm 0.38) \times 10^{-11}$	$(5.97 \pm 0.36) \times 10^{-3}$	$(5.68 \pm 0.29) \times 10^{-4}$	$(6.16 \pm 0.29) \times 10^{-4}$
		3	1.37	1	$(1.32 \pm 0.08) \times 10^{-11}$	$(4.63 \pm 0.18) \times 10^{-11}$	$(4.81 \pm 0.34) \times 10^{-3}$	$(2.82 \pm 0.14) \times 10^{-4}$	$(3.29 \pm 0.14) \times 10^{-4}$
		3	1.37	2	$(1.11 \pm 0.31) \times 10^{-11}$	$(4.09 \pm 0.54) \times 10^{-11}$	$(5.03 \pm 1.53) \times 10^{-3}$	$(2.41 \pm 0.41) \times 10^{-4}$	$(2.89 \pm 0.40) \times 10^{-4}$
		5	1.36	1	$(3.36 \pm 0.11) \times 10^{-11}$	$(8.33 \pm 0.19) \times 10^{-11}$	$(3.36 \pm 0.13) \times 10^{-3}$	$(5.61 \pm 0.15) \times 10^{-4}$	$(6.08 \pm 0.14) \times 10^{-4}$
		5	1.36	2	$(3.08 \pm 0.06) \times 10^{-11}$	$(7.11 \pm 0.87) \times 10^{-11}$	$(3.13 \pm 0.39) \times 10^{-3}$	$(4.69 \pm 0.65) \times 10^{-4}$	$(5.16 \pm 0.65) \times 10^{-4}$

1420	1	1	1.36	1	$(1.83 \pm 0.13) \times 10^{-11}$	$(8.39 \pm 0.69) \times 10^{-11}$	$(6.21 \pm 0.68) \times 10^{-3}$	$(2.79 \pm 0.13) \times 10^{-4}$	$(3.02 \pm 0.13) \times 10^{-4}$
		1	1.36	2	$(1.74 \pm 0.11) \times 10^{-11}$	$(7.94 \pm 0.56) \times 10^{-11}$	$(6.20 \pm 0.59) \times 10^{-3}$	$(2.62 \pm 0.10) \times 10^{-4}$	$(2.86 \pm 0.10) \times 10^{-4}$
		2.5	1.33	1	$(1.46 \pm 0.04) \times 10^{-11}$	$(6.82 \pm 0.28) \times 10^{-11}$	$(6.20 \pm 0.31) \times 10^{-3}$	$(2.20 \pm 0.05) \times 10^{-4}$	$(2.44 \pm 0.05) \times 10^{-4}$
		2.5	1.33	2	$(1.09 \pm 0.02) \times 10^{-11}$	$(6.53 \pm 0.09) \times 10^{-11}$	$(7.99 \pm 0.18) \times 10^{-3}$	$(2.10 \pm 0.02) \times 10^{-4}$	$(2.33 \pm 0.02) \times 10^{-4}$
		4	1.34	1	$(1.91 \pm 0.05) \times 10^{-11}$	$(9.85 \pm 0.10) \times 10^{-11}$	$(6.93 \pm 0.19) \times 10^{-3}$	$(3.34 \pm 0.02) \times 10^{-4}$	$(3.58 \pm 0.02) \times 10^{-4}$
		4	1.34	2	$(1.92 \pm 0.02) \times 10^{-11}$	$(9.16 \pm 0.35) \times 10^{-11}$	$(6.40 \pm 0.25) \times 10^{-3}$	$(3.08 \pm 0.07) \times 10^{-4}$	$(3.32 \pm 0.07) \times 10^{-4}$

[a]Radius determined as the distance from the center along the measured oxygen isotope compositional profile.

[b]Profiles with ID of 1 are shown in Fig. 1.

[c]α_{CO} obtained assuming P_{H2O} of 3×10^{-5} and 1×10^{-4} Pa in the system.

[d]The weighted average of D estimated from experiments at $P_{CO} = 0.5$ and 1 Pa was assumed. See the text for more details.

[e]All the errors represent 2-sigma standard error.

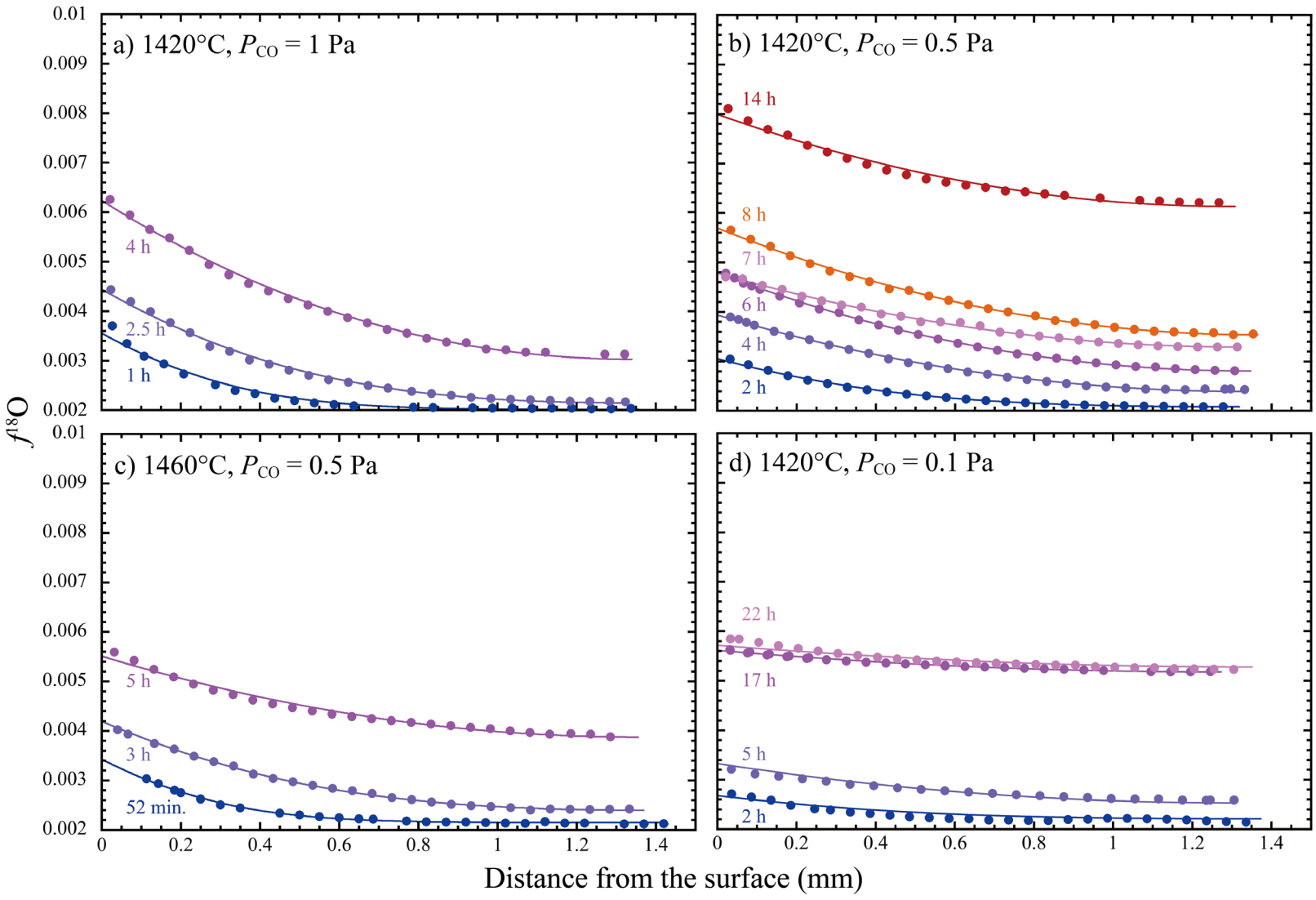

Fig. 1. Typical profiles of oxygen isotopic composition ($f^{18}O$) of samples heated for different duration at (a) 1420°C and P_{CO} = 1 Pa, (b) 1420°C and P_{CO} = 0.5 Pa, (c) 1460°C and P_{CO} = 0.5 Pa, and (d) 1420°C and P_{CO} = 0.1 Pa as a function of distance from the surface to the center. Symbols are the measured data, and solid curves represent the best-fitted profiles by Eq. (2). For the fitting of data at P_{CO} of 0.1 Pa, the weighted average of oxygen self-diffusion coefficient (D) estimated from the profiles shown in (a)–(c) was assumed (see text for details). The rest of the profiles are shown in Fig. S1.

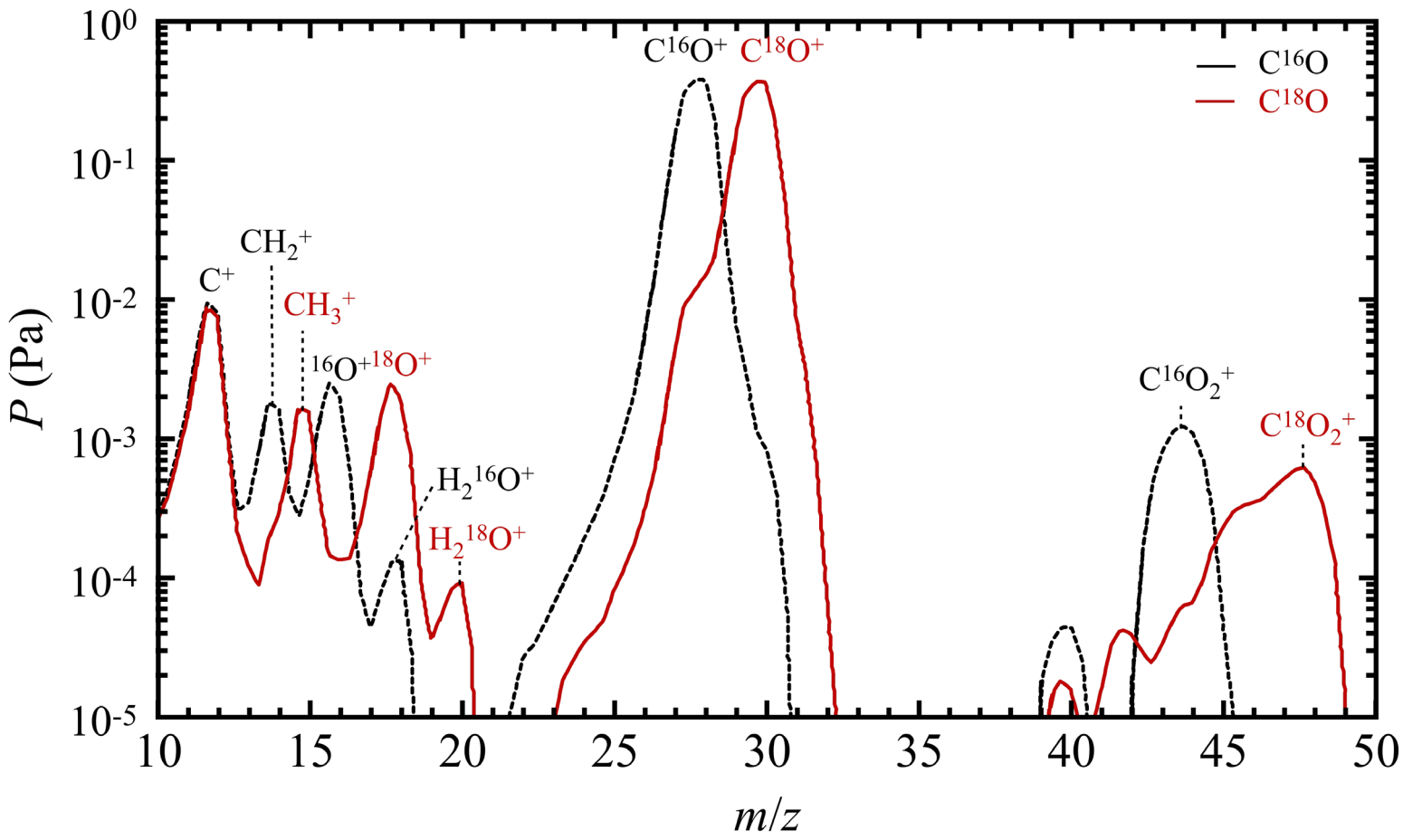

Fig. 2. Typical QMS spectra measured at 1420°C and 0.5 Pa of $C^{16}O$ (black dotted curve) and $C^{18}O$ (red solid curve). Possible major ion species are shown with spectra peaks. A prominent peak at m/z = 20 attributed to $H_2{}^{18}O^+$ was only observed for the experiments with $C^{18}O$ gas.

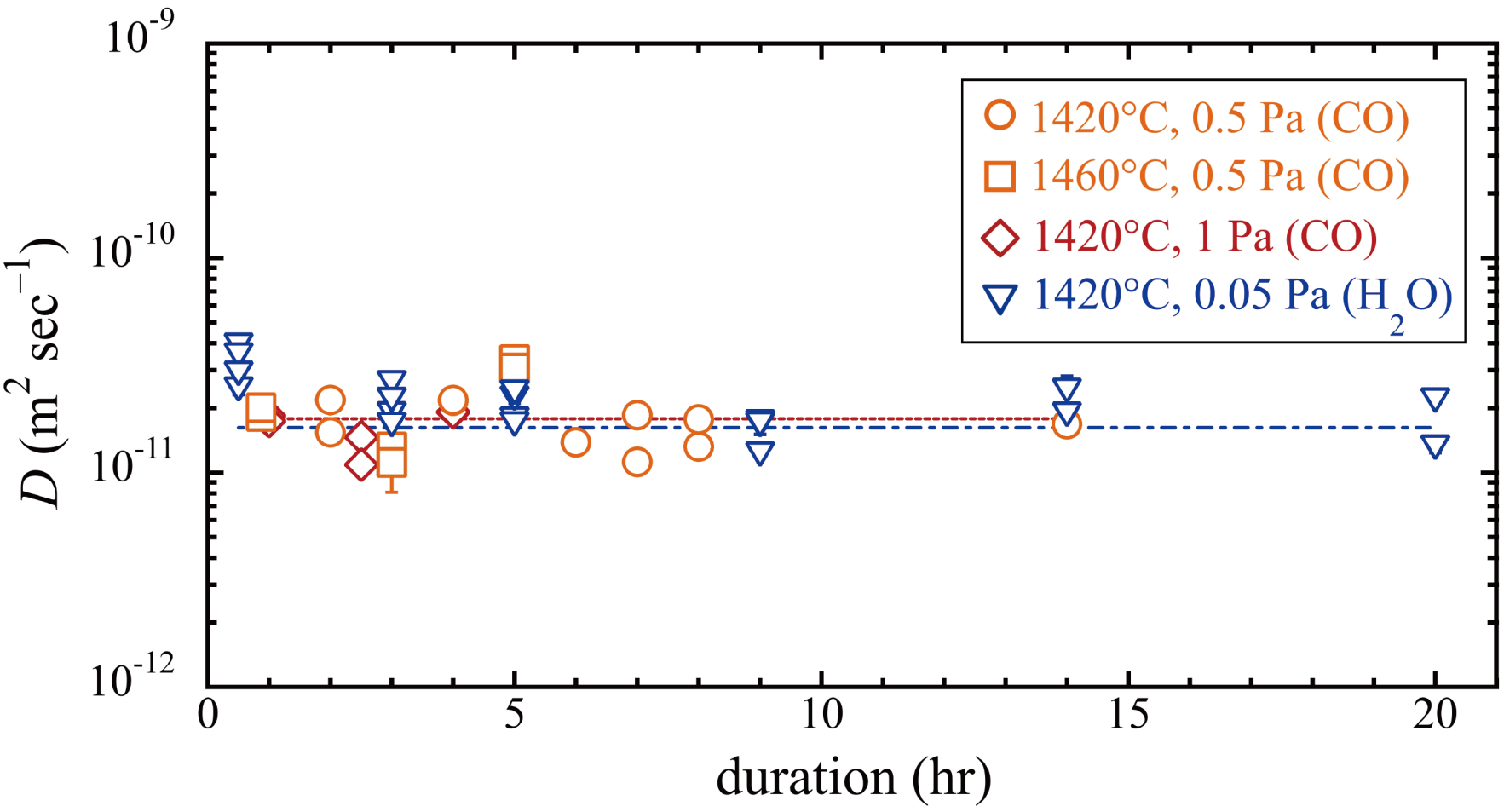

Fig. 3. Diffusion coefficients (D) obtained from the samples heated at 1420°C and P_{CO} = 0.5 Pa (open orange circles), 1460°C and P_{CO} = 0.5 Pa (open orange squares), and 1420°C and P_{CO} = 1 Pa (open red diamond) as a function of heating duration. A dotted red line represents the weighted average of D in this study (1.78×10^{-11} m^2 s^{-1}). The values of D obtained through the oxygen isotope exchange reaction between CAI melt and $H_2{}^{18}O$ of 0.05 Pa (Yamamoto et al., 2021) are shown as open blue triangles with their weighted average (1.62×10^{-11} m^2 s^{-1}; blue dot-dashed line) for comparison. Errors are 2-sigma standard error, most of which are smaller than each symbol size.

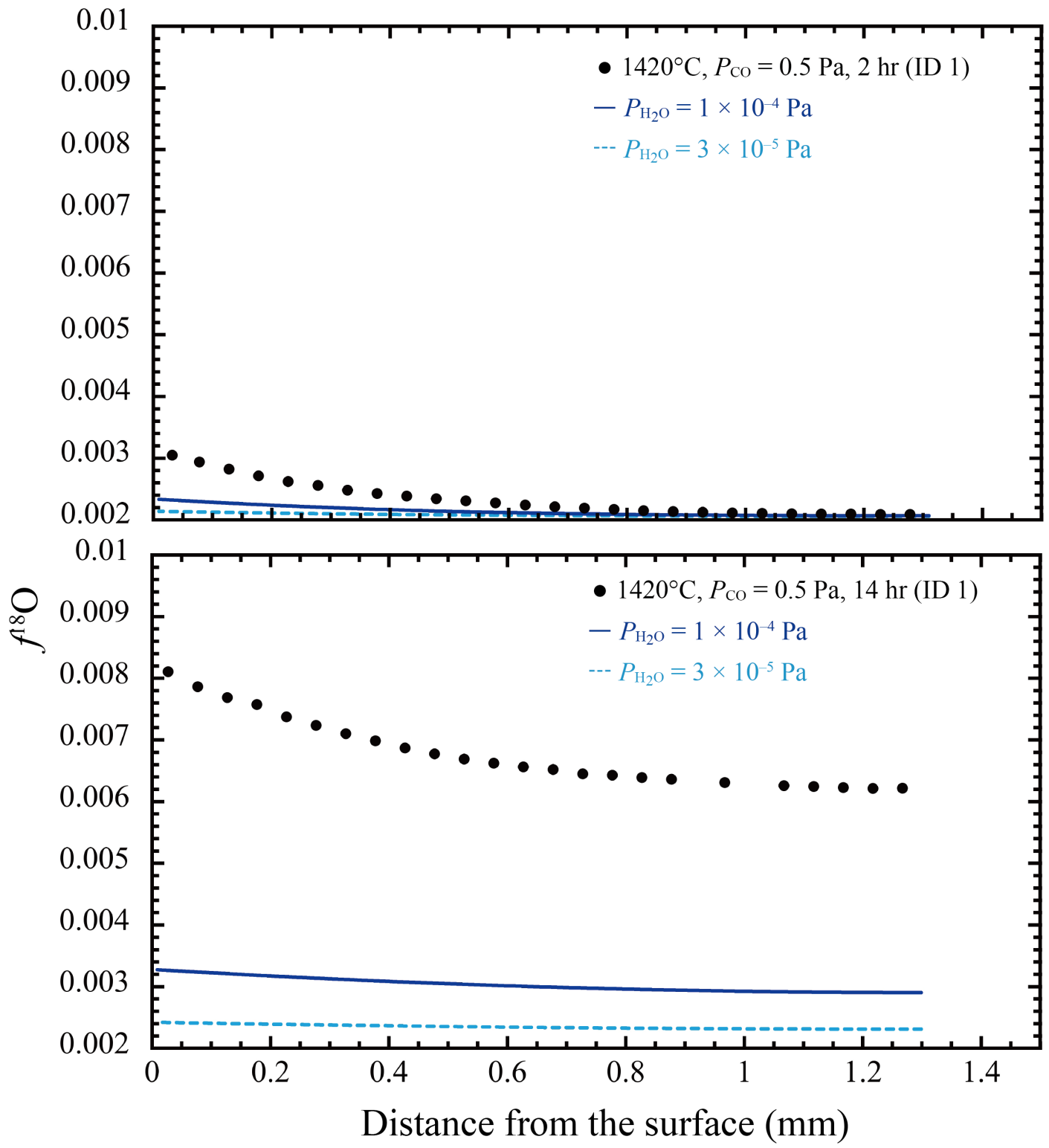

Fig. 4. Comparison between the experimental data of the samples heated for the shortest duration of 2 h (top) and the longest duration of 14 h (bottom) at 1420°C and P_{CO} = 0.5 Pa (closed symbols). Modeled profiles for isotope exchange with ^{18}O-enriched H_2O ($f^{18}O$ =0.98) with pressure of 1×10^{-4} and 3×10^{-5} Pa (dark blue solid curve, light blue dashed curve, respectively) calculated based on Yamamoto et al. (2021) are also shown. The experimental $f^{18}O$ profiles cannot be explained by the oxygen isotope exchange alone with $H_2{}^{18}O$ in the system.

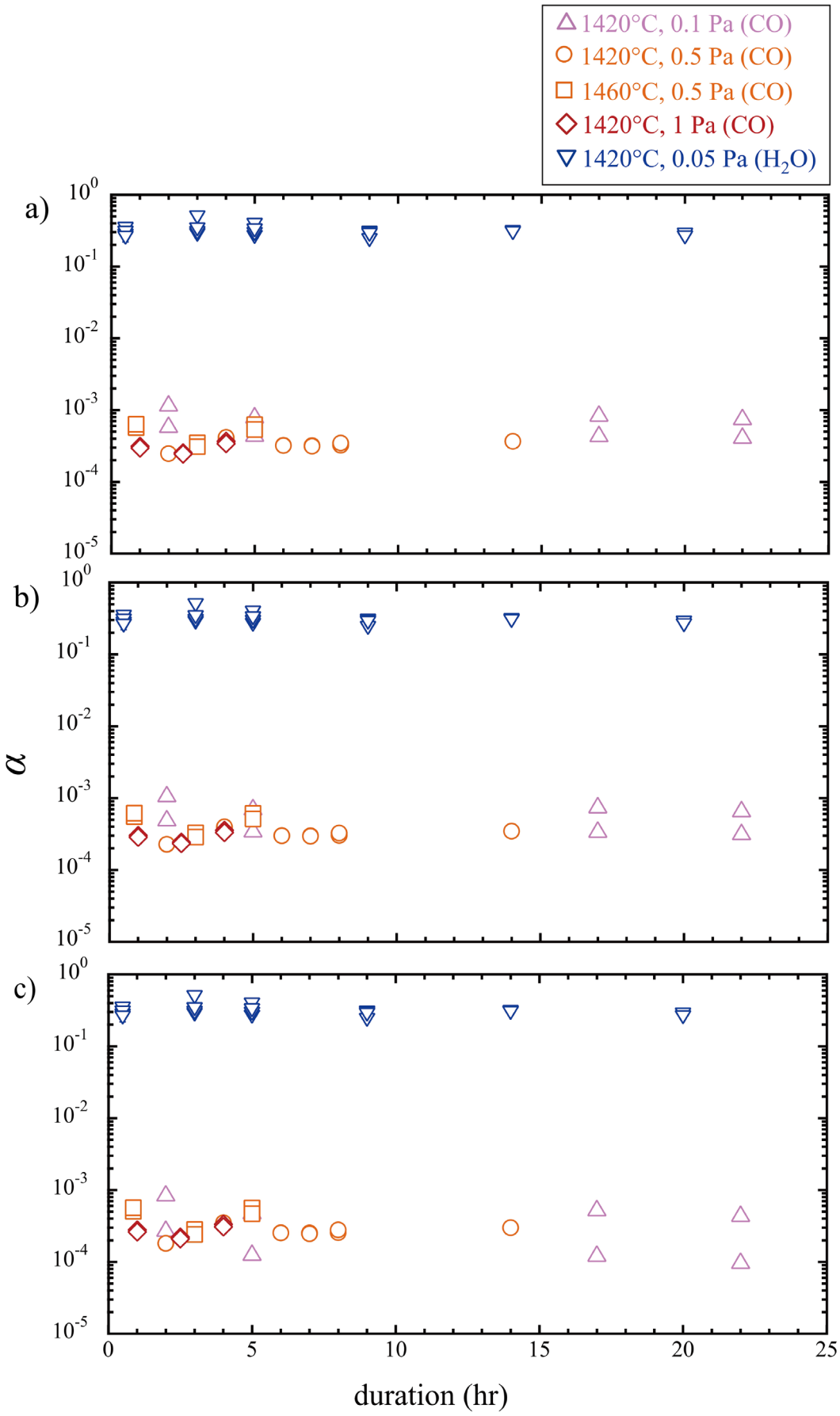

Fig. 5. Isotope exchange efficiency of colliding CO gas at the melt surface (α_{CO}) estimated by the isotope exchange experiments at 1420°C and P_{CO} = 0.1 Pa (open pink up-pointing triangles), 1420°C and P_{CO} = 0.5 Pa (open orange circles), 1460°C and P_{CO} = 0.5 Pa (open orange squares), and 1420°C and P_{CO} = 1 Pa (open red diamond) with (a) no effect of $H_2{}^{18}O$ gas, (b) the effect of 3×10^{-5} Pa of $H_2{}^{18}O$ gas, and (c) the effect of 1×10^{-4} Pa of $H_2{}^{18}O$ gas. The values of α for H_2O (α_{H2O}) as reported in Yamamoto et al. (2021) are shown as open blue down-pointing triangles for comparison. 2-sigma standard errors are smaller than each symbol size.

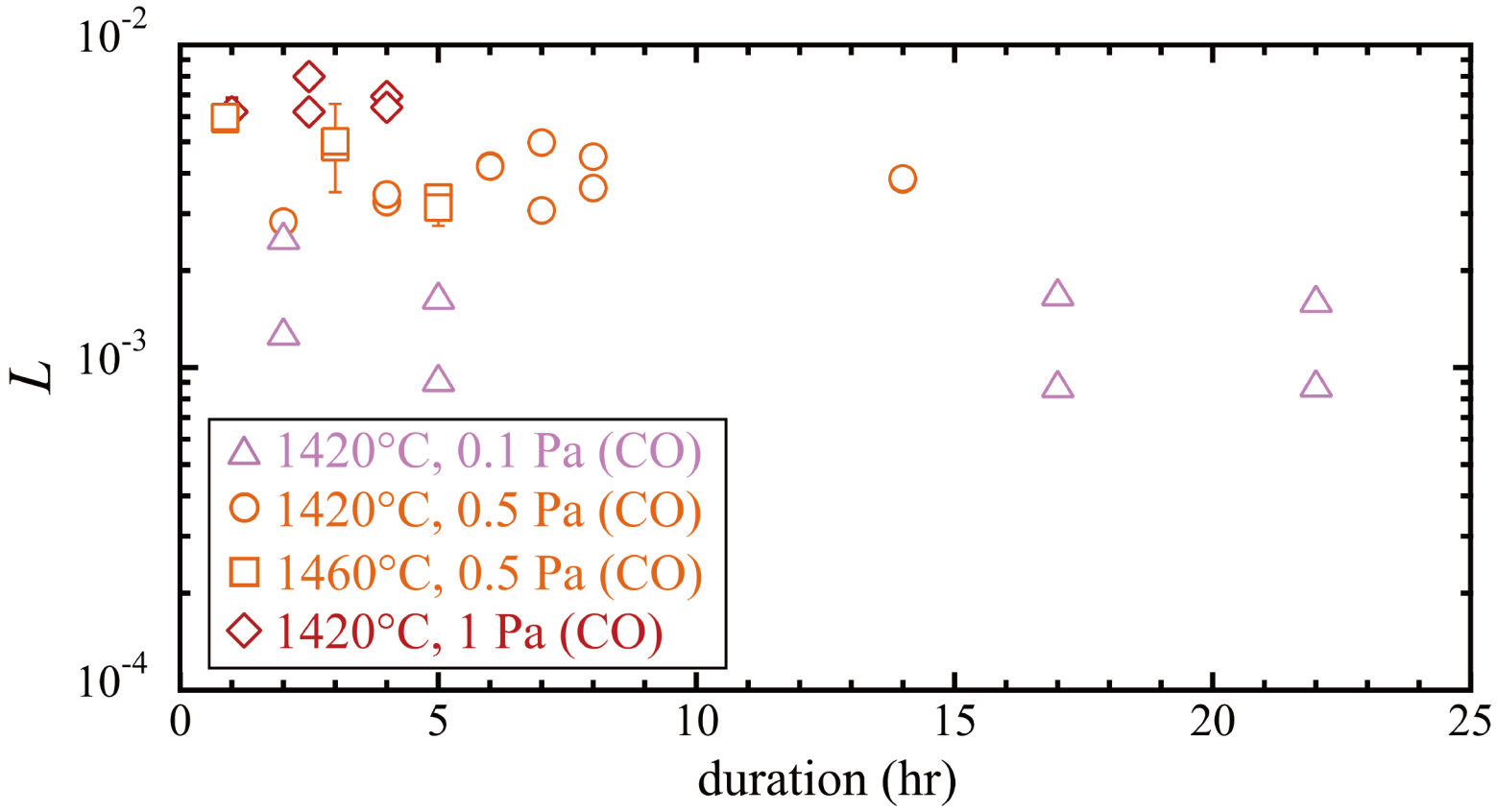

Fig. 6. Dimensionless parameter L (Eq. (4)) for samples heated at 1420°C and P_{CO} = 0.1 Pa (open pink up-pointing triangles), 1420°C and P_{CO} = 0.5 Pa (open orange circles), 1460°C and P_{CO} = 0.5 Pa (open orange squares), and 1420°C and P_{CO} = 1 Pa (open red diamond) as a function of heating duration. Errors bars represent 2-sigma standard errors, most of which are smaller than each symbol size.

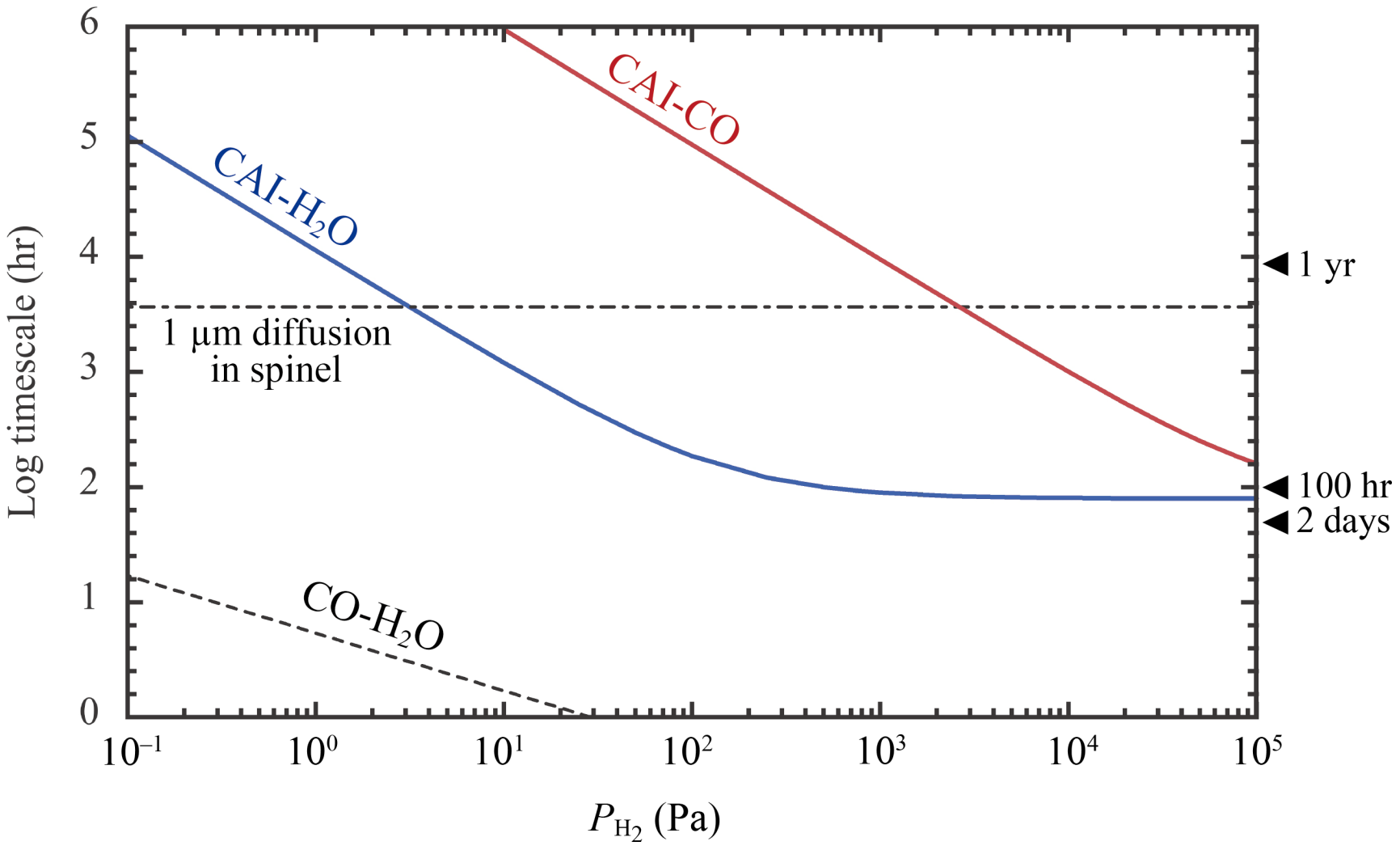

Fig. 7. Timescales of oxygen isotope exchange reactions in the CAI melt-CO-H_2O system at 1420°C as a function of hydrogen partial pressure (P_{H2}) for a 1 cm-diameter spherical CAI melt. Solar composition ratios (P_{H2O} / P_{H2} = P_{CO} /P_{H2} = 10^{-3}) were used to express the horizontal axis as P_{H2}. Timescales required for CAI melt to reach the exchange fraction (x) of 0.9 with CO for α_{CO} of 3.3×10^{-4} are shown as a red solid curve. The blue solid curve represents the timescale for the reaction between CAI melt and H_2O for x = 0.9 (Yamamoto et al., 2021), and the black dashed line shows the oxygen isotope equilibrium timescale between H_2O and CO (Alexander, 2004). The time required for oxygen diffusion of 1 μm into spinel from their surface is based on the oxygen self-diffusion coefficient by Ryerson and McKeegan (1994) (black dot-dashed line).